

SOGS: Second-Order Anchor for Advanced 3D Gaussian Splatting

Jiahui Zhang¹ Fangneng Zhan^{2,3} Ling Shao⁴ Shijian Lu¹
¹Nanyang Technological University ²Harvard University ³MIT
⁴UCAS-Terminus AI Lab, University of Chinese Academy of Sciences
 jiahui003@e.ntu.edu.sg fnzhan@seas.harvard.edu
 ling.shao@ieee.org shijian.lu@ntu.edu.sg

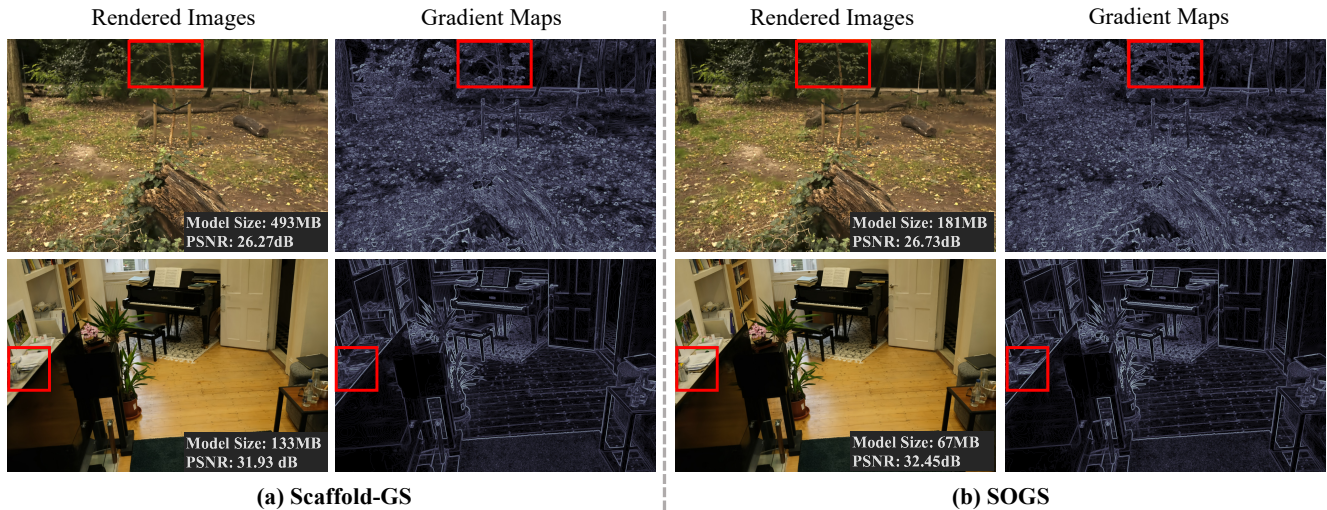


Figure 1. The proposed SOGS can render high-quality textures and geometries and reduce model size simultaneously. The illustrations in (a) and (b) show *Rendered Images* and *Gradient Maps* which are produced by Scaffold-GS [25] and SOGS, respectively, for the samples ‘Stump’ and ‘Room’ from Mip-NeRF360 [2]. The *Gradient Maps* are extracted with the Sobel operator which highlight the texture and geometry of imaged scenes.

Abstract

Anchor-based 3D Gaussian splatting (3D-GS) exploits anchor features in 3D Gaussian prediction, which has achieved impressive 3D rendering quality with reduced Gaussian redundancy. On the other hand, it often encounters the dilemma among anchor features, model size, and rendering quality – large anchor features lead to large 3D models and high-quality rendering whereas reducing anchor features degrades Gaussian attribute prediction which leads to clear artifacts in the rendered textures and geometries. We design SOGS, an anchor-based 3D-GS technique that introduces second-order anchors to achieve superior rendering quality and reduced anchor features and model size simultaneously. Specifically, SOGS incorporates covariance-based second-order statistics and corre-

lation across feature dimensions to augment features within each anchor, compensating for the reduced feature size and improving rendering quality effectively. In addition, it introduces a selective gradient loss to enhance the optimization of scene textures and scene geometries, leading to high-quality rendering with small anchor features. Extensive experiments over multiple widely adopted benchmarks show that SOGS achieves superior rendering quality in novel view synthesis with clearly reduced model size.

1. Introduction

3D scene representation and rendering have been a pivotal task in 3D computer vision, playing a crucial role in various applications such as virtual reality and scene simulation. Neural radiance fields (NeRFs) [27] and its variants [1–3, 46] have been developed to model implicit

*Shijian Lu is the corresponding author.

scene representation and enable volume rendering for high-quality novel view synthesis. However, NeRF is limited by long training and rendering times, largely due to the time-consuming point sampling in volume rendering. Recently, 3D Gaussian Splatting (3D-GS) [18] has been proposed as an alternative which learns explicit 3D scene representations with learnable 3D Gaussians. By leveraging efficient splatting and rasterization, 3D-GS projects 3D Gaussians onto a 2D plane, enabling real-time rendering. However, 3D-GS stacks substantial 3D Gaussians to fit each training view individually, often overlooking the underlying scene structure [25].

The recent Scaffold-GS [25] exploits scene geometry to guide the distribution of 3D Gaussians, reducing Gaussian redundancy and delivering impressive 3D rendering performance. Specifically, it introduces anchor points to store features and exploits MLPs to predict Gaussian attributes from these anchor features. However, Scaffold-GS struggles to strike a balance between rendering quality and model size. Specifically, adopting large anchor features improves rendering quality [9] but it significantly enlarges model size due to the large number of anchor points used in scene representations. Using smaller anchor features can shrink the model, but it clearly degrades the prediction of Gaussian attributes which further leads to suboptimal rendering with various artifacts in rendered textures and geometries. HAC [9] introduces grid-based context modeling and entropy encoding to compress the Scaffold-GS. However, HAC does not reduce the model size but the storage size of the trained Scaffold-GS.

We design SOGS, an innovative anchor-based 3D-GS technique that introduces second-order anchors and achieves superior rendering quality with reduced anchor feature dimensions and model size. Specifically, SOGS incorporates covariance-based second-order statistics to model correlation across anchor feature dimensions. The rationale is that textures and geometries are defined by not only individual features but also the correlation across features. Hence, the correlation across anchor features can effectively guide to capture the pattern of intricate local textures and structures in each anchor. This nice feature enables anchor feature augmentation, empowering SOGS to achieve superior rendering quality with reduced feature dimensions and feature size.

Additionally, we design a selective gradient loss to enhance the rendering quality with small anchor features. This loss computes gradient maps from both the rendered image and the corresponding ground truth that highlight their differences in scene textures and structures. With the difference of the gradient maps, the 3D Gaussian prediction can adaptively focus on image regions where the texture and geometry are hard to render. This enables dynamic region selection along the training process, where the model can

adjust the focused image regions dynamically according to the evolving errors between the gradient maps of the rendered image and the ground truth. Experiments show that SOGS simultaneously achieves superior rendering quality in novel view synthesis as well as clearly reduced model sizes as shown in Fig. 1.

The major contributions of this work can be summarized in three aspects. *First*, we propose SOGS, an innovative anchor-based 3D-GS that introduces second-order anchors to balance the rendering quality and model size. With covariance-based second-order statistics that model correlation across anchor feature dimensions to capture intricate textural and structural patterns, SOGS achieves anchor feature augmentation which produces superior rendering quality with significantly reduced anchor feature dimensions. *Second*, we design a selective gradient loss that guides 3D Gaussian prediction to focus on difficult-to-render textures and structures adaptively, further enhancing rendering quality with small anchor features *Third*, experiments over multiple benchmarks show that SOGS achieves superior novel view synthesis with efficient anchor size and model size, and outperforms the state-of-the-art in rendering quality.

2. Related Work

2.1. Radiance Field and Neural Rendering

Radiance field has been widely explored for novel view synthesis and achieved impressive rendering quality. Neural radiance field (NeRF) [27] utilizes MLPs to learn implicit 3D scene representations from multi-view posed 2D images. Coupled with differentiable volume rendering, NeRF achieves high-quality rendering with superb multi-view consistency. Several NeRF variants have been developed to address various new challenges, including large-scale scenes [32, 33, 37], dynamic scenes [12, 14, 31], few-shot setting [6, 34, 40], pose-free setting [4, 8, 22, 43, 44], and antialiasing [2, 3]. However, NeRF and its variants still suffer from extremely long training and rendering times due to the time-consuming sampling required for volume rendering. Several studies [7, 15, 28, 29] have been proposed to address this issue. For instance, Müller et al. [28] introduce multi-resolution hash encoding to reduce the size of neural networks, significantly shortening the training time and enabling real-time rendering in tens of milliseconds. However, these methods often suffer from degraded reconstruction accuracy and rendering quality of scenes.

Kerbl et al. recently propose 3D Gaussian splatting (3D-GS) [18], which achieves high-quality and real-time rendering by explicitly representing scenes by using parameterized 3D Gaussians, along with efficient splatting and rasterization. Building on its excellent performance, numerous 3D-GS variants have been developed to address diverse challenges and tasks, such as dynamic scenes [21, 23, 26,

36, 41], autonomous driving [38, 47], rendering quality optimization [11, 39, 42, 45], sparse-view setting [5, 10, 20] and colmap-free setting [13], and 3D style transfer [24].

2.2. Anchor-based 3D Gaussian Splatting

One major constraint in 3D-GS is that it stacks a large number of 3D Gaussians to match each training view separately, often overlooking the underlying scene geometry. To address this issue, Lu et al. [25] present Scaffold-GS, the first anchor-based 3D-GS technique that incorporates anchor points to predict Gaussian attributes through multi-layer perceptrons (MLPs). Scaffold-GS leverages scene structure to guide the distribution of 3D Gaussians, reducing Gaussian redundancy and delivering impressive 3D rendering performance. However, Scaffold-GS faces challenges in balancing enhanced rendering quality with anchor and model size reduction. Although several follow-ups [9, 35] introduce context-based entropy encoding to compress the Scaffold-GS, they reduce its storage size instead of anchor and model sizes as used during training and rendering. The proposed SOGS introduces second-order anchors, enabling superior rendering quality with reduced model size.

3. Proposed Method

We propose SOGS, a novel anchor-based 3D Gaussian splatting that introduces second-order anchors and selective gradient loss to achieve superior rendering quality with reduced anchor and model sizes. Fig. 2 shows the overview of SOGS. The 3D Gaussian splatting [18] (3D-GS) and Scaffold-GS [25] (the base model for our SOGS) are briefly introduced in Sec. 3.1. In Sec. 3.2, we first explain why the proposed second-order anchor enables the model to enhance rendering quality in reduced anchor and model sizes, and then describe the details of the second-order anchor. Besides, to further ensure high-quality image rendering under compact anchor size, we design a selective gradient loss, detailed in Sec. 3.3.

3.1. Preliminaries

3D Gaussian Splatting (3D-GS). 3D-GS [18] explicitly represents scenes using anisotropic 3D Gaussians and enables real-time rendering through efficient differentiable splatting. 3D Gaussians are initialized from point clouds generated by structure-from-motion [16, 30]. Each Gaussian is defined by a covariance matrix, a position (mean), an opacity value α , and spherical harmonics coefficients representing color c , where the covariance matrix is decomposed into scaling matrix and rotation matrix to facilitate differentiable optimization.

For rendering, 3D Gaussians are projected onto a 2D plane through splatting, followed by α -blending. Specifically, the color C of a pixel is computed by blending N or-

dered 2D Gaussians overlapping that pixel, formulated as:

$$C = \sum_{n \in N} c_n \alpha_n \prod_{z=1}^{n-1} (1 - \alpha_z), \quad (1)$$

where c_n and α_n represent the color and opacity of the n -th 2D Gaussian.

Scaffold-GS. Scaffold-GS [25] introduces anchor points to predict 3D Gaussians via MLPs. It aims to leverage scene geometry to guide the distribution and attributes of 3D Gaussians and reduce the Gaussian redundancy. Specifically, Scaffold-GS voxelizes the entire scene based on the point cloud initialized by COLMAP [30] and assigns the center of each voxel as an anchor point. A local scene feature $\mathbf{f}^a \in \mathbb{R}^D$, a scaling factor \mathbf{l}^a and K offsets $\mathbf{o}^a \in \mathbb{R}^{3K}$ are stored in each anchor as the anchor attributes. Given an anchor position \mathbf{x}_a , its relative distance δ_{ac} and viewing direction \mathbf{d}_{ac} to a camera position \mathbf{x}_c can be represented as: $\delta_{ac} = \|\mathbf{x}_a - \mathbf{x}_c\|_2$, $\mathbf{d}_{ac} = \frac{\mathbf{x}_a - \mathbf{x}_c}{\|\mathbf{x}_a - \mathbf{x}_c\|_2}$. The prediction of K Gaussians from one anchor point using MLPs F can then be formulated as follows:

$$\{\alpha_k, c_k, q_k, s_k\}_{k=1}^K = F(\mathbf{f}^a, \delta_{ac}, \mathbf{d}_{ac}), \quad (2)$$

where α_k , c_k , s_k and q_k denote the opacity, color, scaling and the rotation-related quaternion of the k -th Gaussian, respectively. The positions of the K Gaussians are calculated by this formula:

$$\{p_k\}_{k=1}^K = \mathbf{x}_a + \{o_k^a\}_{k=1}^K * \mathbf{l}^a. \quad (3)$$

Scaffold-GS follows the same rendering process as Eq. 1 described in 3D-GS after predicting the Gaussian attributes.

3.2. Second-Order Anchor

In this section, we first explain why the proposed second-order anchor enables the model to achieve superior image rendering with compact anchor size. The key lies in leveraging covariance-based second-order feature statistics to achieve anchor feature augmentation. Specifically, second-order feature statistics extract co-varying relationships across anchor feature dimensions. As textures and structures are defined not only by individual features but also by their interdependencies, these co-varying relationships can guide the capture of intricate local textural and structural patterns within each anchor, facilitating feature augmentation. As a result, SOGS compensates for the reduced feature dimensions and ensures superior rendering quality by performing feature augmentation. We provide the visualization of the impact of second-order anchors on scene textures and structures in the Sec. 4.5.

Given anchor feature set $\mathbf{F}^a \in \mathbb{R}^{N \times D} = [\mathbf{f}_1^a, \mathbf{f}_2^a, \dots, \mathbf{f}_N^a]$, where N and D denote the number of

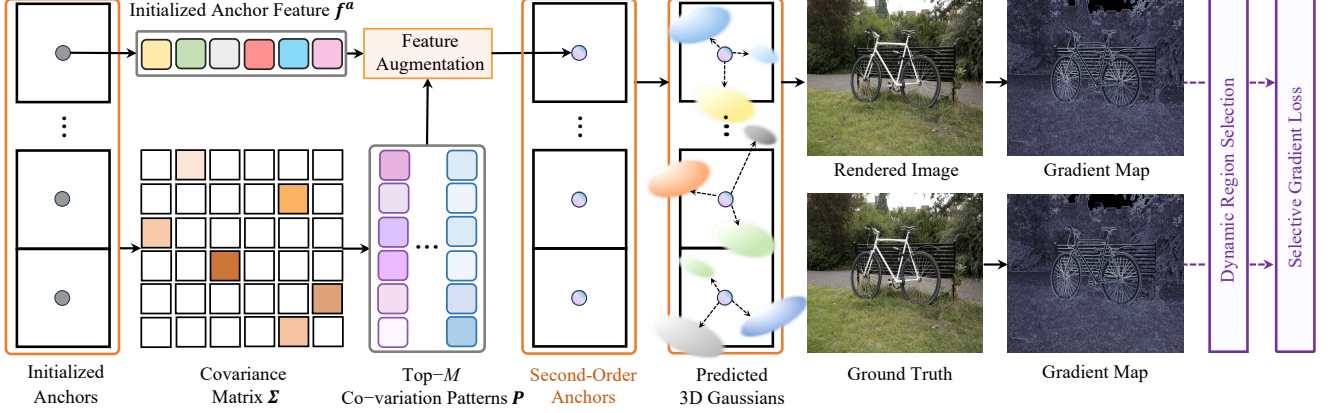


Figure 2. **Overview of the proposed SOGS.** Initialized from point clouds, each anchor stores an anchor feature vector $\mathbf{f}^a \in \mathbb{R}^D$. Putting \mathbf{f}^a along D dimensions as D variables and all anchors as observed samples, the second-order anchor statistics capturing co-varying relations across D can be computed from the covariance matrix Σ across D dimensions. We select the top M eigenvectors \mathbf{P} as the most significant co-variation patterns and combine \mathbf{P} with \mathbf{f}^a to capture anchor-specific textures and geometries for anchor feature augmentation, second-order anchor construction and Gaussian prediction. With the gradient maps of the rendered image and the ground truth, the selective gradient loss guides to learn to render finer textures and geometries with dynamic region selection.

anchors and the dimensionality of each anchor feature, we first compute second-order statistics in the anchor feature set. Specifically, we treat D feature dimensions (channels) as D variables and utilize the anchor set as N observation samples, and compute the covariance matrix $\Sigma \in \mathbb{R}^{D \times D}$ across these channels, which can be formulated as:

$$\Sigma = \frac{1}{N-1} (\mathbf{F}^a - \boldsymbol{\mu}^T)(\mathbf{F}^a - \boldsymbol{\mu}^T)^T, \quad (4)$$

$$\boldsymbol{\mu} = \frac{1}{N} \mathbf{F}^a, \quad (5)$$

where $\boldsymbol{\mu} \in \mathbb{R}^D$ denotes the mean vector across N samples, used for feature centering. Given that two variables with large variances can yield a large covariance despite only weak relationship, we then construct a correlation matrix \mathbf{R} from the covariance matrix Σ to standardize the relationships among D variables, eliminating the influence of different scales or variances:

$$\mathbf{R} = \mathbf{A}^{-1} \Sigma \mathbf{A}^{-1}, \quad (6)$$

$$\mathbf{A} = \text{diag}(\sigma_1, \dots, \sigma_u, \dots, \sigma_D), \quad \sigma_u = \sqrt{\Sigma_{uu}} \quad (7)$$

where \mathbf{A} is a diagonal matrix and the diagonal elements are the standard deviation of D variables. The correlation between u -th and v -th variables can then be expressed as:

$$R_{uv} = \frac{\Sigma_{uv}}{\sigma_u \sigma_v}, \quad (8)$$

where Σ_{uv} represents the covariance between the u -th and v -th variables. With \mathbf{R} , we extract M principle co-varying

relationships across anchor feature dimensions. Specifically, we perform eigendecomposition and decompose the matrix \mathbf{R} into the eigenvector matrix $\mathbf{Q} \in \mathbb{R}^{D \times D}$ and the diagonal matrix $\Lambda \in \mathbb{R}^{D \times D}$ of eigenvalues:

$$\mathbf{R} = \mathbf{Q} \Lambda \mathbf{Q}^T, \quad (9)$$

where \mathbf{Q} is an orthogonal matrix and each column is an eigenvector representing a co-variation pattern across anchor feature dimensions. We sort the eigenvalues in descending order, where the eigenvector corresponding to the largest eigenvalue captures the most significant co-variation patterns across the feature dimensions. Following this, we select the top- M eigenvectors $\mathbf{P} = [\mathbf{P}_1, \dots, \mathbf{P}_M]$ from \mathbf{Q} as the primary directions of co-variation.

We then leverage \mathbf{P} to guide the extraction of textural and structural information in each anchor. As the co-varying relationships across anchor feature dimensions are extracted from the anchor set \mathbf{F}^a , we treat \mathbf{P} as the global-shared co-variations. Combined with the feature \mathbf{f}^a in one anchor, we can capture the anchor-specific textures and structures as follows:

$$\mathbf{f}_i^t = F_i([\mathbf{P}_i, \mathbf{f}^a]), \quad i \in [1, M], \quad (10)$$

where $F_i(\cdot)$ represents the two-layer MLP used to extract the textures and structures for anchor \mathbf{f}^a based on the i -th principal co-varying relationship across anchor feature dimensions. Finally, we concatenate the extracted features with the original anchor feature to achieve feature augmentation and predict Gaussian attributes. Take one second-order anchor as an example:

$$\{\alpha_k, c_k, q_k, s_k\}_{k=0}^K = F(\mathbf{f}^a, \{\mathbf{f}_i^t\}_{i=0}^M, \boldsymbol{\delta}_{ac}, \mathbf{d}_{ac}). \quad (11)$$

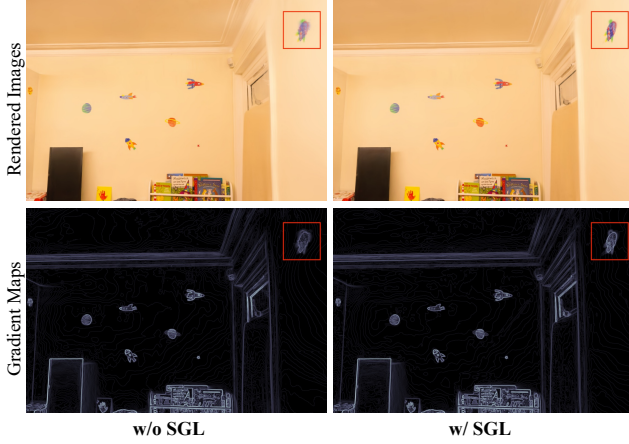


Figure 3. **Visual illustration of the proposed selective gradient loss (SGL)**. SGL clearly improves the rendering quality by generating finer textures and details. **Zoom in for best view.**

Note that $\{f_i^t\}_{i=0}^M$ are derived from f^a for feature augmentation and do not increase the anchor feature dimensions and the size of each anchor.

3.3. Selective Gradient Loss

In addition to proposing second-order anchors for anchor feature augmentation to achieve superior rendering quality with reduced anchor size, we design a selective gradient loss to further ensure the rendering quality under compact anchor features. It enables the model to adaptively identify difficult-to-render textures and structures, and regularize Gaussian prediction corresponding to these regions. With the designed loss, superior rendering quality with finer textures can be achieved as shown in Fig 3. Given the limited sensitivity of pixel-level L1 loss to textures and structures in RGB images, we consider gradient map to emphasize textural and structural regions. Specifically, we exploit the Sobel operator to extract horizontal and vertical gradient maps (G'_x, G'_y, G_x, G_y) of the rendering result $I' \in \mathbb{R}^{H \times W \times C}$ and its corresponding ground truth I , which can be expressed as follows:

$$\begin{aligned} G'_x &= S_x * I', & G'_y &= S_y * I', \\ G_x &= S_x * I, & G_y &= S_y * I, \end{aligned} \quad (12)$$

$$S_x = \begin{bmatrix} -1 & 0 & 1 \\ -2 & 0 & 2 \\ -1 & 0 & 1 \end{bmatrix}, \quad S_y = \begin{bmatrix} -1 & -2 & -1 \\ 0 & 0 & 0 \\ 1 & 2 & 1 \end{bmatrix}, \quad (13)$$

where S_x and S_y denote the horizontal and vertical Sobel kernels, respectively. We then use Euclidean metric to measure the horizontal and vertical gradient discrepancies (l_x, l_y) between the rendering I' and the corresponding ground

truth I , which are then averaged to derive the final discrepancies as follows:

$$\begin{aligned} l_x &= \frac{1}{\sqrt{HW}} \sum_{x=0}^{H-1} \sum_{y=0}^{W-1} |G'_x(x, y) - G_x(x, y)|, \\ l_y &= \frac{1}{\sqrt{HW}} \sum_{x=0}^{H-1} \sum_{y=0}^{W-1} |G'_y(x, y) - G_y(x, y)|. \end{aligned} \quad (14)$$

Gradient maps, derived from differences in pixel intensities, typically exhibit meaningful gradients in localized regions, such as edges and areas with significant intensity changes, which are crucial for capturing structures and textures. In contrast, the majority of areas in gradient map comprise flat and low-gradient regions with limited information. Therefore naively adopting the horizontal and vertical gradient discrepancies as the loss function can cause low-gradient regions to dominate the overall loss. As a result, the model may deemphasize regions critical for preserving fine textures and structures, focusing instead on less important flat areas. Besides, the regions with meaningful gradients should also be distinguished, prioritizing greater attention to textures and structures exhibiting larger rendering errors. To address the above issues, we introduce a dynamic region selection that computes the rendering error map as a weight map, defined by the absolute difference between the gradient maps of the rendered result and the ground truth, which can be expressed by:

$$\begin{aligned} w_x &= |G'_x(x, y) - G_x(x, y)|, \\ w_y &= |G'_y(x, y) - G_y(x, y)|. \end{aligned} \quad (15)$$

Combined with the horizontal and vertical weight maps, the selective gradient loss \mathcal{L}_s can be formulated as:

$$\mathcal{L}_s = w_x * l_x + w_y * l_y, \quad (16)$$

Based on the above analysis, the selective gradient loss enables the model to focus on the difficult-to-render textural and structural regions adaptively. Besides, the model is able to adjust the focused regions dynamically in response to the evolving rendering error map throughout the training process. Note, the pixel-level L1 loss with D-SSIM term between RGB images is also used in the training process, which complements the proposed selective gradient loss used between gradient maps. And we also keep the volume regularization as described in Scaffold-GS [25]. The total loss function is given as follows:

$$\mathcal{L} = \lambda_1 \mathcal{L}_1 + \lambda_{SSIM} \mathcal{L}_{SSIM} + \lambda_{vol} \mathcal{L}_{vol} + \lambda_s \mathcal{L}_s, \quad (17)$$

where the $\lambda_s, \lambda_1, \lambda_{SSIM}$ and λ_{vol} represent the training weights of the selective gradient loss \mathcal{L}_s , the L1 loss \mathcal{L}_1 , the D-SSIM term \mathcal{L}_{SSIM} and the volume regularization \mathcal{L}_{vol} .

Datasets	Mip-NeRF360				Tanks&Temples				Deep Blending			
Methods	SSIM [↑]	PSNR [↑]	LPIPS [↓]	Anchor Size	SSIM [↑]	PSNR [↑]	LPIPS [↓]	Anchor Size	SSIM [↑]	PSNR [↑]	LPIPS [↓]	Anchor Size
Scaffold-GS	0.806	27.50	0.252	32 dim	0.853	23.96	0.177	32 dim	0.906	30.21	0.254	32 dim
SOGS(Ours)	0.815	27.85	0.221	16 dim	0.855	24.14	0.176	12 dim	0.907	30.29	0.252	12 dim

Table 1. **Quantitative comparisons** of novel view synthesis. All methods are trained with the same training data. SOGS achieves superior rendering quality with reduced anchor (model) size. Notably, SOGS using the feature dimension of 12 can still outperform the Scaffold-GS that uses a feature dimension of 32. We do not compare with HAC [9] and ContextGS [35], as they leverage compression techniques to reduce the storage size of Scaffold-GS rather than the actual anchor and model sizes as used in training and rendering.

Datasets	BungeeNeRF			
Methods	SSIM [↑]	PSNR [↑]	LPIPS [↓]	Anchor Size
Scaffold-GS	0.865	26.62	0.241	32 dim
SOGS(Ours)	0.880	27.06	0.171	16 dim

Table 2. **Quantitative comparisons** on large-scale scenes from the dataset BungeeNeRF [37]. All methods are trained with the same training data.

4. Experiments

4.1. Datasets and Implementation Details

Datasets For both training and testing, we adopt the datasets and configurations in Scaffold-GS [25] and conduct experiments on images of 19 real-world scenes. Specifically, we evaluate SOGS across all nine scenes from the Mip-NeRF360 dataset [2], two scenes from the Tanks&Temples dataset [19], and two additional scenes from the Deep Blending dataset [17]. These scenes exhibit diverse styles, ranging from bounded indoor environments to unbounded outdoor ones. We also evaluate SOGS on the BungeeNeRF dataset [37], which includes six large-scale outdoor scenes, to further validate its effectiveness. The datasets are divided into training and test sets following the same settings as Scaffold-GS, with image resolutions consistent with those used in Scaffold-GS.

Implementation For the second-order anchor, we reduce the dimension D of the anchor features in Scaffold-GS from 32 to 16, or even to 12. The covariance matrix Σ is computed from all anchors in scene representations which captures the global correlation across all anchor feature dimensions. The number of the selected eigenvectors is set to $M = 2$. All MLPs used to extract anchor-specific textual and structural information consist of two layers with ReLU activation. For the loss function, the training weights λ_s , λ_1 , λ_{SSIM} and λ_{vol} are set to 0.01, 0.8, 0.2 and 0.01. Please note, for fair comparisons, we keep the loss terms λ_1 , λ_{SSIM} and λ_{vol} the same as in Scaffold-GS. The number of

3D Gaussians corresponding to one second-order anchor is set as $K = 10$. We use the Pytorch framework to implement SOGS. The SOGS model is trained for 30000 iterations, the same as Scaffold-GS and 3D-GS.

4.2. Comparisons with the State-of-the-Art

We primarily compare SOGS with Scaffold-GS [25] over datasets Mip-NeRF360, Tank&Temple and Deep Blending as Scaffold-GS is an anchor-based 3D Gaussian splatting method and is most relevant to our study. Table 1 shows experimental results over the same test images as described in Section 4.1. We can observe that SOGS outperforms Scaffold-GS consistently in PSNR, SSIM and LPIPS across all evaluated scenes. The anchor size of SOGS is reduced to 16 in the dataset Mip-NeRF360, while it is challengingly reduced to 12 in Tank&Temple and Deep Blending. The superior performance is largely attributed to our proposed second-order anchor which performs anchor feature augmentation to compensate for the reduced anchor feature size and improve the rendering quality as well as the selective gradient loss that further ensures the high-quality rendering under small-sized anchor features. Further, we benchmark SOGS with Scaffold-GS over the BungeeNeRF dataset which provides diverse large-scale scenes. It can be observed that SOGS achieves superior rendering quality with only 16-dimensional anchors. Besides, as shown in Fig. 4, we perform the visual comparison of SOGS with 3D-GS and Scaffold-GS and provide their model sizes in each scene. With the compact anchor size of the proposed second-order anchor, SOGS achieves a significant reduction in model size while delivering superior novel view synthesis with much less artifacts but finer details. Note we did not compare with HAC [9] and ContextGS [35] as they compress the storage size of Scaffold-GS rather than the actual model size as used in training and rendering.

4.3. Ablation Studies

We conduct extensive ablation experiments to validate the effectiveness of the proposed second-order anchor and the selective gradient loss. In the experiments, we keep the model size and anchor feature dimension the same as used

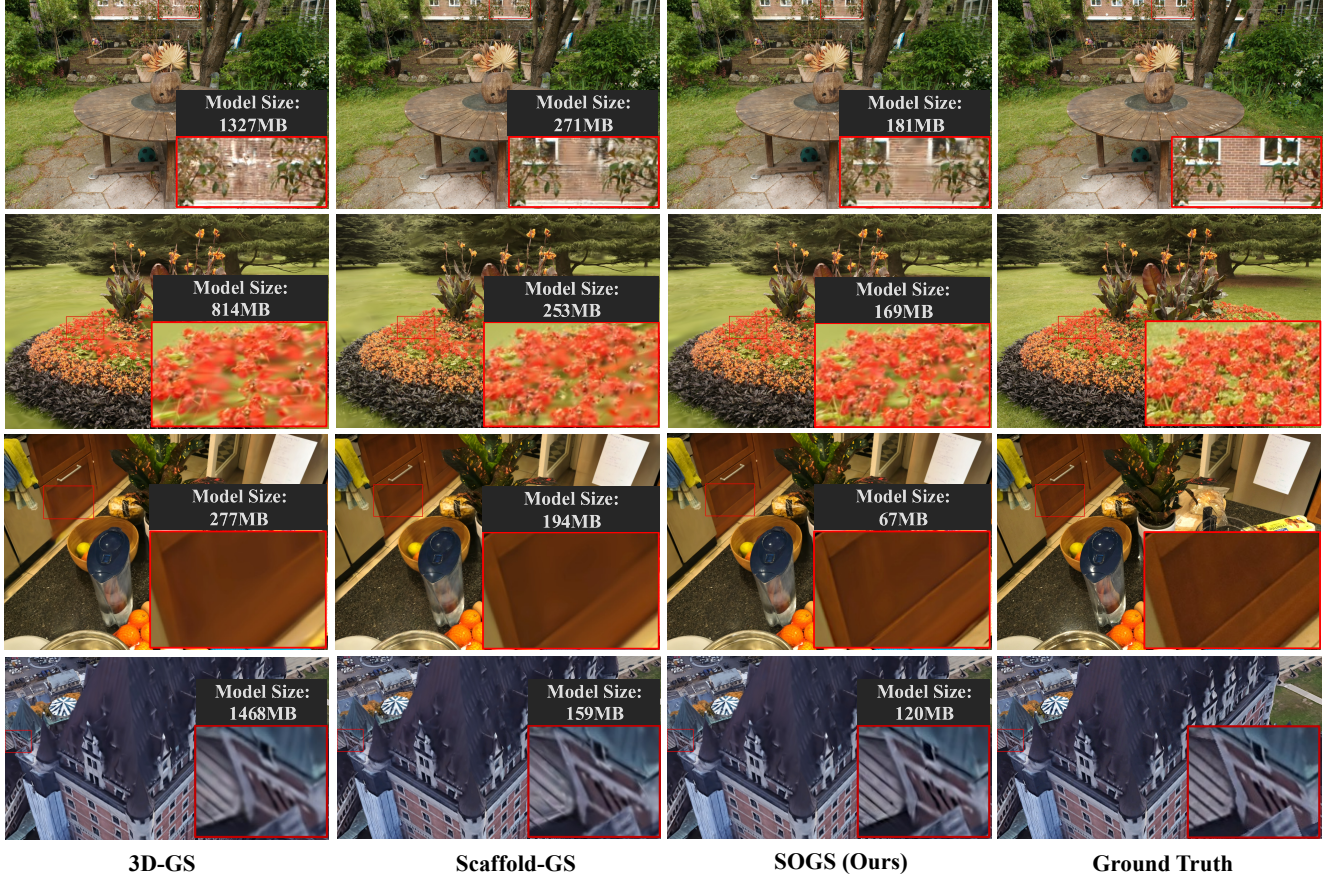


Figure 4. **Qualitative comparisons of SOGS with 3D-GS [18] and Scaffold-GS [25].** SOGS achieves smaller model size and superior image rendering with much less artifacts but more fine details. The experiments are conducted over multiple indoor and outdoor scenes including ‘Garden’, ‘Flower’ and ‘Counter’ from the Mip-NeRF360 and ‘Quebec’ from the BungeeNeRF. **Zoom in for best view.**

Models	Evaluation Metrics		
	PSNR \uparrow	SSIM \uparrow	LPIPS \downarrow
Base	26.62	0.865	0.241
Base+SOA	27.25	0.879	0.208
Base+SOA+SGL	27.39	0.887	0.161

Table 3. **Ablation studies of SOGS** on the dataset BungeeNeRF. With Scaffold-GS as the baseline *Base*, *Base+SOA* introduces the second-order anchor to augment anchor features which clearly improves the Gaussian attribute prediction and image rendering. *Base+SOA+SGL* (i.e., SOGS) further introduces the selective gradient loss which enables the Gaussian prediction to focus on regions with difficult-to-render textures and geometries. All models are trained under the same settings and model size, and the anchor feature dimension is set at 32.

in Scaffold-GS, aiming to screen out other variations and show how our two designs improve the rendering quality.

More details are described in the following two subsections.

Second-order Anchor We first examine how our proposed second-order anchor affects PSNR, SSIM and LPIPS. In this experiment, we adopt the Scaffold-GS as the baseline model *Base* that performs anchor-based Gaussian splatting with naive anchors. On top of the *Base*, we train a model *Base+SOA* that incorporates our proposed second-order anchor to replace the naive anchor in Scaffold-GS. As Table 3 shows, *Base+SOA* outperforms the *Base* clearly in PSNR, SSIM and LPIPS, indicating that the second-order anchor can effectively improve the Gaussian attribute prediction and novel view synthesis by anchor feature augmentation.

Selective Gradient Loss To evaluate how the proposed selective gradient loss contributes, we train a new model *Base+SOA+SGL* (i.e., the complete SOGS) that incorporates the selective gradient loss on top of *Base+SOA*. Table 3 shows experimental results. We can observe that

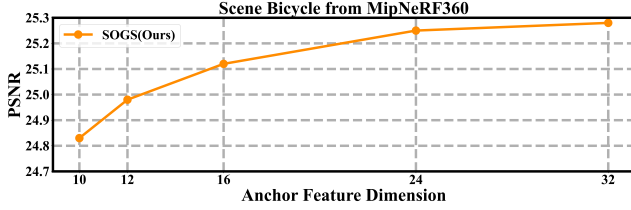


Figure 5. **Anchor feature dimension vs SOGS performance:** The performance of SOGS varies with the feature dimension D in each anchor, where increasing D improves SOGS consistently together with the increased model size and computational cost. The graph shows the PSNR of the scene ‘Bicycle’ from MipNeRF360.

Base+SOA+SGL further improves the novel view synthesis consistently across all three evaluation metrics, demonstrating its effectiveness on Gaussian attribute prediction and rendering quality.

4.4. Parameter Investigation

We examine how the dimension of anchor features D affects the SOGS performance. Fig. 5 shows experiments on the scene ‘Bicycle’ from the dataset MipNeRF360. We can observe that the performance of SOGS (in PSNR \uparrow score) improves consistently while the feature dimension D increases. Specifically, the feature dimension plays a vital role in the rendering quality as it sets the upper bound for the encoded information as well as the effectiveness of feature augmentation in SOGS. As D becomes larger than 16, the performance gains gradually diminish due to feature saturation while the model size and computational costs grow greatly. We therefore set D at 12 or 16 in our implemented system to balance the model size and performance.

4.5. Visualization

We visualize the impact of second-order anchors on scene textures and structures. As Fig. 6 shows, our proposed second-order anchor can enhance the rendered images with finer structures and textures. This visualization verifies that the proposed second-order anchor can effectively capture the structural and textural patterns for anchor feature augmentation, and facilitate subsequent Gaussian prediction and image rendering with augmented features.

5. Conclusion

This paper presents SOGS, an innovative anchor-based 3D Gaussian splatting technique that incorporates second-order anchors to achieve superior rendering with compact anchor feature dimensions and model size. Specifically, by introducing covariance-based second-order statistics, SOGS learns correlations across anchor feature dimensions to capture anchor-specific textures and structural patterns. This

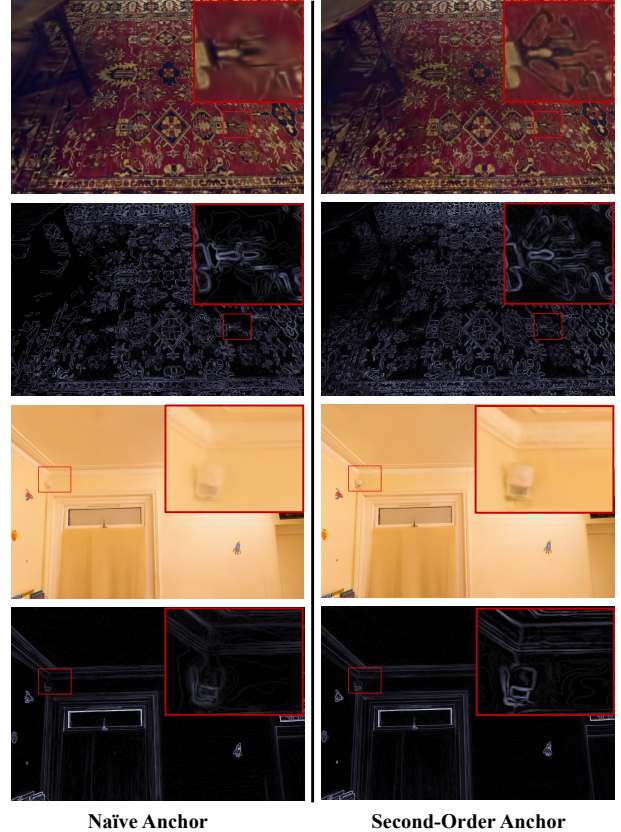


Figure 6. **Visualization of the impact of second-order anchors on scene textures and structures.** The two samples are ‘Drjohnson’ and ‘Playroom’ from dataset Deep Blending [17]. The proposed second-order anchor improves the rendering quality with superior structures and textures by anchor feature augmentation. **Zoom in for best view.**

enables each anchor to achieve feature augmentation, compensating for the reduced anchor feature size and resulting in superior Gaussian prediction and rendering quality. Besides, we also design a selective gradient loss to further ensure high-quality rendering under compact anchor features, which enables the model to dynamically focus on the Gaussian prediction for difficult-to-render textural and structural regions. Experiments over multiple widely adopted indoor and outdoor scenes show that SOGS achieves superior novel view synthesis with compact model size. Although time complexity increases slightly due to the additional computations in second-order anchors, SOGS still achieves efficient training and real-time rendering.

6. Acknowledgements

This project is funded by the Ministry of Education Singapore, under the Tier-2 project scheme with a project number MOE-T2EP20220-0003.

References

- [1] Jonathan T Barron, Ben Mildenhall, Matthew Tancik, Peter Hedman, Ricardo Martin-Brualla, and Pratul P Srinivasan. Mip-nerf: A multiscale representation for anti-aliasing neural radiance fields. In *Proceedings of the IEEE/CVF International Conference on Computer Vision*, pages 5855–5864, 2021. 1
- [2] Jonathan T Barron, Ben Mildenhall, Dor Verbin, Pratul P Srinivasan, and Peter Hedman. Mip-nerf 360: Unbounded anti-aliased neural radiance fields. In *Proceedings of the IEEE/CVF Conference on Computer Vision and Pattern Recognition*, pages 5470–5479, 2022. 1, 2, 6
- [3] Jonathan T Barron, Ben Mildenhall, Dor Verbin, Pratul P Srinivasan, and Peter Hedman. Zip-nerf: Anti-aliased grid-based neural radiance fields. In *Proceedings of the IEEE/CVF International Conference on Computer Vision*, pages 19697–19705, 2023. 1, 2
- [4] Wenjing Bian, Zirui Wang, Kejie Li, Jia-Wang Bian, and Victor Adrian Prisacariu. Nope-nerf: Optimising neural radiance field with no pose prior. In *Proceedings of the IEEE/CVF Conference on Computer Vision and Pattern Recognition*, pages 4160–4169, 2023. 2
- [5] David Charatan, Sizhe Lester Li, Andrea Tagliasacchi, and Vincent Sitzmann. pixelsplat: 3d gaussian splats from image pairs for scalable generalizable 3d reconstruction. In *Proceedings of the IEEE/CVF Conference on Computer Vision and Pattern Recognition*, pages 19457–19467, 2024. 3
- [6] Anpei Chen, Zexiang Xu, Fuqiang Zhao, Xiaoshuai Zhang, Fanbo Xiang, Jingyi Yu, and Hao Su. Mvsnerf: Fast generalizable radiance field reconstruction from multi-view stereo. In *Proceedings of the IEEE/CVF International Conference on Computer Vision*, pages 14124–14133, 2021. 2
- [7] Anpei Chen, Zexiang Xu, Andreas Geiger, Jingyi Yu, and Hao Su. Tensorf: Tensorial radiance fields. In *European Conference on Computer Vision*, pages 333–350. Springer, 2022. 2
- [8] Yue Chen, Xingyu Chen, Xuan Wang, Qi Zhang, Yu Guo, Ying Shan, and Fei Wang. Local-to-global registration for bundle-adjusting neural radiance fields. In *Proceedings of the IEEE/CVF Conference on Computer Vision and Pattern Recognition*, pages 8264–8273, 2023. 2
- [9] Yihang Chen, Qianyi Wu, Jianfei Cai, Mehrtash Harandi, and Weiyao Lin. Hac: Hash-grid assisted context for 3d gaussian splatting compression. *arXiv preprint arXiv:2403.14530*, 2024. 2, 3, 6
- [10] Yuedong Chen, Haofei Xu, Chuanxia Zheng, Bohan Zhuang, Marc Pollefeys, Andreas Geiger, Tat-Jen Cham, and Jianfei Cai. Mvsplat: Efficient 3d gaussian splatting from sparse multi-view images. *arXiv preprint arXiv:2403.14627*, 2024. 3
- [11] Kai Cheng, Xiaoxiao Long, Kaizhi Yang, Yao Yao, Wei Yin, Yuexin Ma, Wenping Wang, and Xuejin Chen. Gaussianpro: 3d gaussian splatting with progressive propagation. In *Forty-first International Conference on Machine Learning*, 2024. 3
- [12] Yilun Du, Yanan Zhang, Hong-Xing Yu, Joshua B Tenenbaum, and Jiajun Wu. Neural radiance flow for 4d view synthesis and video processing. In *Proceedings of the IEEE/CVF International Conference on Computer Vision*, pages 14324–14334, 2021. 2
- [13] Zhiwen Fan, Wenyan Cong, Kairun Wen, Kevin Wang, Jian Zhang, Xinghao Ding, Danfei Xu, Boris Ivanovic, Marco Pavone, Georgios Pavlakos, et al. Instantsplat: Unbounded sparse-view pose-free gaussian splatting in 40 seconds. *arXiv preprint arXiv:2403.20309*, 2024. 3
- [14] Chen Gao, Ayush Saraf, Johannes Kopf, and Jia-Bin Huang. Dynamic view synthesis from dynamic monocular video. In *Proceedings of the IEEE/CVF International Conference on Computer Vision*, pages 5712–5721, 2021. 2
- [15] Stephan J Garbin, Marek Kowalski, Matthew Johnson, Jamie Shotton, and Julien Valentin. Fastnerf: High-fidelity neural rendering at 200fps. In *Proceedings of the IEEE/CVF International Conference on Computer Vision*, pages 14346–14355, 2021. 2
- [16] Richard Hartley and Andrew Zisserman. *Multiple view geometry in computer vision*. Cambridge university press, 2003. 3
- [17] Peter Hedman, Julien Philip, True Price, Jan-Michael Frahm, George Drettakis, and Gabriel Brostow. Deep blending for free-viewpoint image-based rendering. *ACM Transactions on Graphics (ToG)*, 37(6):1–15, 2018. 6, 8
- [18] Bernhard Kerbl, Georgios Kopanas, Thomas Leimkühler, and George Drettakis. 3d gaussian splatting for real-time radiance field rendering. *ACM Transactions on Graphics (ToG)*, 42(4):1–14, 2023. 2, 3, 7
- [19] Arno Knapitsch, Jaesik Park, Qian-Yi Zhou, and Vladlen Koltun. Tanks and temples: Benchmarking large-scale scene reconstruction. *ACM Transactions on Graphics (ToG)*, 36(4):1–13, 2017. 6
- [20] Jiahe Li, Jiawei Zhang, Xiao Bai, Jin Zheng, Xin Ning, Jun Zhou, and Lin Gu. Dngaussian: Optimizing sparse-view 3d gaussian radiance fields with global-local depth normalization. In *Proceedings of the IEEE/CVF Conference on Computer Vision and Pattern Recognition*, pages 20775–20785, 2024. 3
- [21] Zhan Li, Zhang Chen, Zhong Li, and Yi Xu. Spacetime gaussian feature splatting for real-time dynamic view synthesis. In *Proceedings of the IEEE/CVF Conference on Computer Vision and Pattern Recognition*, pages 8508–8520, 2024. 2
- [22] Chen-Hsuan Lin, Wei-Chiu Ma, Antonio Torralba, and Simon Lucey. Barf: Bundle-adjusting neural radiance fields. In *Proceedings of the IEEE/CVF International Conference on Computer Vision*, pages 5741–5751, 2021. 2
- [23] Youtian Lin, Zuozhuo Dai, Siyu Zhu, and Yao Yao. Gaussian-flow: 4d reconstruction with dynamic 3d gaussian particle. In *Proceedings of the IEEE/CVF Conference on Computer Vision and Pattern Recognition*, pages 21136–21145, 2024. 2
- [24] Kunhao Liu, Fangneng Zhan, Muyu Xu, Christian Theobalt, Ling Shao, and Shijian Lu. Stylegaussian: Instant 3d style transfer with gaussian splatting. In *SIGGRAPH Asia 2024 Technical Communications*, pages 1–4. 2024. 3
- [25] Tao Lu, Mulin Yu, Linning Xu, Yuanbo Xiangli, Limin Wang, Dahua Lin, and Bo Dai. Scaffold-gs: Structured 3d gaussians for view-adaptive rendering. In *Proceedings of*

- the IEEE/CVF Conference on Computer Vision and Pattern Recognition*, pages 20654–20664, 2024. 1, 2, 3, 5, 6, 7
- [26] Zhicheng Lu, Xiang Guo, Le Hui, Tianrui Chen, Min Yang, Xiao Tang, Feng Zhu, and Yuchao Dai. 3d geometry-aware deformable gaussian splatting for dynamic view synthesis. In *Proceedings of the IEEE/CVF Conference on Computer Vision and Pattern Recognition*, pages 8900–8910, 2024. 2
- [27] Ben Mildenhall, Pratul P Srinivasan, Matthew Tancik, Jonathan T Barron, Ravi Ramamoorthi, and Ren Ng. Nerf: Representing scenes as neural radiance fields for view synthesis. In *European conference on computer vision*, pages 405–421. Springer, 2020. 1, 2
- [28] Thomas Müller, Alex Evans, Christoph Schied, and Alexander Keller. Instant neural graphics primitives with a multi-resolution hash encoding. *arXiv preprint arXiv:2201.05989*, 2022. 2
- [29] Christian Reiser, Songyou Peng, Yiyi Liao, and Andreas Geiger. Kilonerf: Speeding up neural radiance fields with thousands of tiny mlps. In *Proceedings of the IEEE/CVF International Conference on Computer Vision*, pages 14335–14345, 2021. 2
- [30] Johannes L Schonberger and Jan-Michael Frahm. Structure-from-motion revisited. In *Proceedings of the IEEE conference on computer vision and pattern recognition*, pages 4104–4113, 2016. 3
- [31] Ruizhi Shao, Zerong Zheng, Hanzhang Tu, Boning Liu, Hongwen Zhang, and Yebin Liu. Tensor4d: Efficient neural 4d decomposition for high-fidelity dynamic reconstruction and rendering. In *Proceedings of the IEEE/CVF Conference on Computer Vision and Pattern Recognition*, pages 16632–16642, 2023. 2
- [32] Matthew Tancik, Vincent Casser, Xinchen Yan, Sabeek Pradhan, Ben Mildenhall, Pratul P Srinivasan, Jonathan T Barron, and Henrik Kretschmar. Block-nerf: Scalable large scene neural view synthesis. In *Proceedings of the IEEE/CVF Conference on Computer Vision and Pattern Recognition*, pages 8248–8258, 2022. 2
- [33] Haithem Turki, Deva Ramanan, and Mahadev Satyanarayanan. Mega-nerf: Scalable construction of large-scale nerfs for virtual fly-throughs. In *Proceedings of the IEEE/CVF Conference on Computer Vision and Pattern Recognition*, pages 12922–12931, 2022. 2
- [34] Guangcong Wang, Zhaoxi Chen, Chen Change Loy, and Ziwei Liu. Sparsenerf: Distilling depth ranking for few-shot novel view synthesis. In *Proceedings of the IEEE/CVF International Conference on Computer Vision*, pages 9065–9076, 2023. 2
- [35] Yufei Wang, Zhihao Li, Lanqing Guo, Wenhan Yang, Alex C Kot, and Bihan Wen. Contextgs: Compact 3d gaussian splatting with anchor level context model. *arXiv preprint arXiv:2405.20721*, 2024. 3, 6
- [36] Guanjun Wu, Taoran Yi, Jiemin Fang, Lingxi Xie, Xiaopeng Zhang, Wei Wei, Wenyu Liu, Qi Tian, and Xinggang Wang. 4d gaussian splatting for real-time dynamic scene rendering. In *Proceedings of the IEEE/CVF Conference on Computer Vision and Pattern Recognition*, pages 20310–20320, 2024. 3
- [37] Yuanbo Xiangli, Linning Xu, Xingang Pan, Nanxuan Zhao, Anyi Rao, Christian Theobalt, Bo Dai, and Dahua Lin. Bungeenerf: Progressive neural radiance field for extreme multi-scale scene rendering. In *European conference on computer vision*, pages 106–122. Springer, 2022. 2, 6
- [38] Yunzhi Yan, Haotong Lin, Chenxu Zhou, Weijie Wang, Haiyang Sun, Kun Zhan, Xianpeng Lang, Xiaowei Zhou, and Sida Peng. Street gaussians for modeling dynamic urban scenes. *arXiv preprint arXiv:2401.01339*, 2024. 3
- [39] Zhiwen Yan, Weng Fei Low, Yu Chen, and Gim Hee Lee. Multi-scale 3d gaussian splatting for anti-aliased rendering. In *Proceedings of the IEEE/CVF Conference on Computer Vision and Pattern Recognition*, pages 20923–20931, 2024. 3
- [40] Jiawei Yang, Marco Pavone, and Yue Wang. Freenerf: Improving few-shot neural rendering with free frequency regularization. In *Proceedings of the IEEE/CVF Conference on Computer Vision and Pattern Recognition*, pages 8254–8263, 2023. 2
- [41] Ziyi Yang, Xinyu Gao, Wen Zhou, Shaohui Jiao, Yuqing Zhang, and Xiaogang Jin. Deformable 3d gaussians for high-fidelity monocular dynamic scene reconstruction. In *Proceedings of the IEEE/CVF Conference on Computer Vision and Pattern Recognition*, pages 20331–20341, 2024. 3
- [42] Zehao Yu, Anpei Chen, Binbin Huang, Torsten Sattler, and Andreas Geiger. Mip-splatting: Alias-free 3d gaussian splatting. In *Proceedings of the IEEE/CVF Conference on Computer Vision and Pattern Recognition*, pages 19447–19456, 2024. 3
- [43] Jiahui Zhang, Fangneng Zhan, Rongliang Wu, Yingchen Yu, Wenqing Zhang, Bai Song, Xiaoqin Zhang, and Shijian Lu. Vmrf: View matching neural radiance fields. In *Proceedings of the 30th ACM International Conference on Multimedia*, pages 6579–6587, 2022. 2
- [44] Jiahui Zhang, Fangneng Zhan, Yingchen Yu, Kunhao Liu, Rongliang Wu, Xiaoqin Zhang, Ling Shao, and Shijian Lu. Pose-free neural radiance fields via implicit pose regularization. In *Proceedings of the IEEE/CVF International Conference on Computer Vision*, pages 3534–3543, 2023. 2
- [45] Jiahui Zhang, Fangneng Zhan, Muyu Xu, Shijian Lu, and Eric Xing. Fregs: 3d gaussian splatting with progressive frequency regularization. In *Proceedings of the IEEE/CVF Conference on Computer Vision and Pattern Recognition*, pages 21424–21433, 2024. 3
- [46] Kai Zhang, Gernot Riegler, Noah Snavely, and Vladlen Koltun. Nerf++: Analyzing and improving neural radiance fields. *arXiv preprint arXiv:2010.07492*, 2020. 1
- [47] Xiaoyu Zhou, Zhiwei Lin, Xiaojun Shan, Yongtao Wang, Deqing Sun, and Ming-Hsuan Yang. Drivinggaussian: Composite gaussian splatting for surrounding dynamic autonomous driving scenes. In *Proceedings of the IEEE/CVF Conference on Computer Vision and Pattern Recognition*, pages 21634–21643, 2024. 3